Energy 301 (2024) 131707

Contents lists available at ScienceDirect

Energy

journal homepage: www.elsevier.com/locate/energy

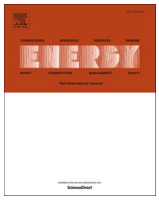

Heat transfer enhancement of a Stirling engine heating tube with three-pronged slant rods under oscillatory flow

Feng Xin [a,b], Bin Tang [a], Bin Zhao [a], Yanfeng Yang [a], Wei Liu [b,*], Zhichun Liu [b,**]

[a] School of Energy and Power Engineering, Changsha University of Science and Technology, Changsha, 410114, China
[b] School of Energy and Power Engineering, Huazhong University of Science and Technology, Wuhan, 430074, China

ARTICLE INFO

Keywords:
Heat transfer enhancement
Oscillatory flow
Three-pronged slant rods
Heating tube
Stirling engine

ABSTRACT

Heaters are crucial components in Stirling engines, where the working medium adsorbed heat from an external heat source. Enhancing heat transfer within the heater is essential for boosting the operational efficiency of the Stirling engine. In this study, a tube equipped with three-pronged slant rods was employed to improve the heat transfer within the heater under conditions of oscillatory flow. Three pairs of dynamic longitudinal vortices were generated and exhibited regular movement patterns with distinct phase angles. In comparison to the smooth tube configuration, the enhanced tube outlet exhibited a notable increase in the average working-medium temperature by 62 K and 46 K during the entry and return stages, respectively. The degree of heat transfer enhancement was found to be contingent upon the pitch, height, and inclination angle of the slant rod. Optimal heat transfer enhancement was achieved with slant rods featuring a pitch of 26 mm, a height of 3.5 mm, and an inclination angle of 45°. The performance evaluation criterion ranged from 1.29 to 1.81 of enhanced tube compared to smooth tube. These findings underscore the effective enhancement of heat transfer facilitated by the three-pronged slant rods within the Stirling engine's heater.

1. Introduction

Stirling engines are external combustion engines that can be fuelled by traditional fossil fuels [1,2] and renewable sources, such as solar energy [3–5], biomass energy [6–8], geothermal energy [9], nuclear power [10,11], and biogas [12]. They offer advantages over internal combustion engines, including low noise levels, simple structures, and high theoretical efficiencies [13,14]. Consequently, they hold immense potential across various applications including combined cooling, heating, and power generation (CCHP) [15,16], underwater power generation [17], space station power supply [18], vehicle hybrids [19,20] and waste heat recovery [21,22].

Currently, Stirling engines have yet to capture a significant market share, primarily owing to their low practical efficiency (less than 40 %) [23]. The main energy loss during Stirling engine operation results from the temperature disparity between the internal working medium and the external heat source. Therefore, enhancing heat transfer in the heaters and coolers is crucial for improving the engine's actual operational efficiency. The temperature difference between the heat source and working medium is notably greater at the hot end than at the cold end. Thus, improving the heat-transfer performance of heaters effectively boosts the energy-utilisation efficiency of Stirling engines [24]. Presently, research on enhancing heater heat transfer has predominantly focused on modifying heat source characteristics [25,26], optimizing working medium operating parameters [27,28], optimizing geometrical parameters of heating tubes [29,30] or tube cluster arrangements [31,32]. Among these, modifications to heat source characteristics or working medium operating parameters may restrict the application environment or conditions of the Stirling engine. Regarding the optimization of heating tube geometrical parameters or tube cluster arrangements, heat transfer enhancement may be limited if optimization is minor, while extensive optimization may significantly increase dead volume.

Several studies have proposed enhancing heat-transfer performance by adopting specific heat-transfer enhancement structures. Given that the working medium inside the heating tube of a Stirling engine is gaseous, heat transfer between the working medium and the heating tube is relatively weak compared to other heat transfer processes of the heater. Therefore, enhancing heat transfer inside the heating tube is crucial. Currently, the heat transfer enhancement technologies are

* Corresponding author.
** Corresponding author.
E-mail addresses: w_liu@hust.edu.cn (W. Liu), zcliu@hust.edu.cn (Z. Liu).

https://doi.org/10.1016/j.energy.2024.131707
Received 28 January 2024; Received in revised form 6 April 2024; Accepted 17 May 2024
Available online 18 May 2024

classified into three types: active [33–35], passive [36,37], and composite [38–40]. Among these, the passive heat transfer enhancement technology has been extensively applied owing to its operation without additional power sources, offering greater convenience and safety [41,42]. Passive heat transfer enhancement inside the tube can be achieved by treating the tube wall surface [43–45], altering the tube shape [46–48], and introducing disturbing device inside tube [49–52]. Notably, the pressure, temperature, and velocity within the Stirling engine heater undergo rapid and uneven changes over time and space, known as oscillatory flow, which differs from the principles governing general steady-state unidirectional flow [53,54]. Thus, it is imperative to consider the specific flow characteristics of the fluid in a Stirling engine heater when developing heat-transfer enhancement technologies.

Currently, research on heat transfer enhancement for Stirling engine heaters under oscillatory flows is limited. Existing studies focus on two main approaches: (i) noncircular cross-section tubes, including triangular cross-section tubes [55], rectangular cross-section tubes [55,56], corrugated groove cross-sections [57]; and (ii) surface treatments of heat transfer such as circumferential slots [55], rectangular fins, semicircular fins, and triangular fins [58]. While these methods improve heat transfer performance to some extent, they predominantly enhance disturbance of the working medium near the sidewall, leaving heat transfer in the core flow region relatively weak. Moreover, altering the cross-sectional shape or wall surface may reduce the high-temperature and high-pressure resistance of the tube wall material. Therefore, there is a need to explore new heat transfer enhancement methods that achieve improved performance without significantly compromising the durability of the tube wall material under high temperatures and pressures.

In our previous studies, the heat transfer of a heater under oscillating flow was improved by adjusting the flow field in the boundary flow region [59,60]. However, achieving a comprehensive enhancement in heat transfer performance could be more effective if the working medium in the tube core region could exchange with that in the boundary region without compromising the endurance of the tube wall material. Building on this analysis, a heating tube with three-pronged slant rods was developed. These rods guide the working medium from the core flow region to the boundary flow region. And the working medium in the boundary flow region would be forced to the core flow region. Consequently, heat transfer enhancement becomes more effective without altering the structure and shape of the tube wall.

Numerical simulations were conducted to investigate the changes in the characteristics of the working medium (i.e., temperature, velocity, and pressure) in the heating tube. The dynamic boundary conditions of heating tube were interpreted into the numerical simulation through implementing user-defined functions to simulate oscillatory flow. The study examined the impact of the geometrical parameters of the slant rod on the heat transfer performance and friction factor of the heating tube under oscillatory flow conditions. The primary objective of this study was to enhance the actual operational efficiency of a Stirling engine by improving the heat transfer capacity of the heater.

2. Physical and mathematical models

2.1. Physical model

Fig. 1 depicts the geometry of the circular heating tube with three-pronged slant rods. The tube wall was rendered transparent to illustrate the structure of the slant rods, despite being fabricated from a non-transparent metal entity. Detailed geometric dimensions are provided in Table 1. The working medium was compressible helium gas, with property parameters changing in real-time during Stirling engine operation.

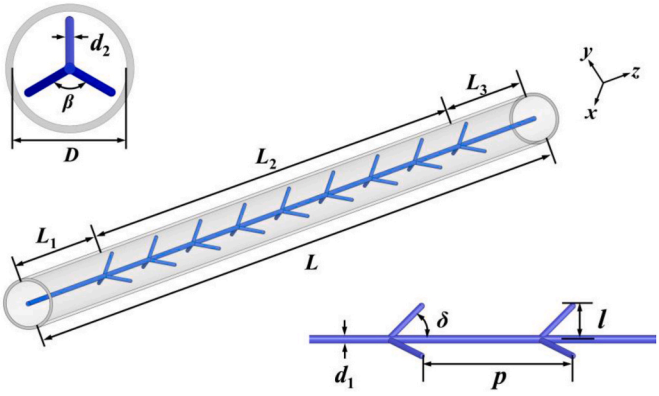

Fig. 1. Schematic diagram of heating tube structure inserting with three-pronged slant rods.

Table 1
Geometrical parameters of the heating tube inserting with three-pronged slant.

Parameters	L	L_1	L_2	L_3	D	d_1	d_2	β
Units	mm	mm	mm	mm	mm	mm	mm	°
Values	300	46	208	46	8	0.8	0.6	120

Parameters	l	p	δ
Units	mm	mm	°
Values	2.5、2.8、3、3.2、3.5	26、42、53、70、105	30、45、60、90、120、135、150

2.2. Mathematical model

2.2.1. Governing equations

The volumetric forces and internal heat sources were not considered in the study. The standard k-ω turbulence model was employed as the computational model. The 3D double-precision solver was utilized. The pressure-governing equation was discretized using the PRESTO! method. The pressure and velocity of working medium were coupled using the PISO algorithm. A time step of 1/360 of the cycles was set for the simulation. The governing equations adopted in numerical simulation were as following:

The continuity equation:

$$\frac{\partial \rho}{\partial t} + \nabla(\rho \vec{u}) = 0 \tag{1}$$

The momentum equation:

$$\rho \frac{\partial \vec{u}}{\partial t} + \nabla \vec{u}(\rho \vec{u}) = -\nabla P - \frac{2}{3}\nabla[\mu(\nabla \vec{u})] + \nabla\left[\mu(\nabla \vec{u})^T\right] + \nabla[\mu(\nabla \vec{u})] \tag{2}$$

The energy equation:

$$\rho c_p \frac{\partial T}{\partial t} + \rho c_p \vec{u} \nabla T = \nabla[\lambda(\nabla T)] + \left[\frac{\partial P}{\partial t} + \vec{u}\nabla P\right] + \Phi \tag{3}$$

The turbulence kinetic energy equation:

$$\frac{\partial}{\partial t}(\rho k) + \frac{\partial}{\partial x_i}(\rho k u_i) = \frac{\partial}{\partial x_i}\left(\Gamma_k \frac{\partial k}{\partial x_i}\right) + G_k - Y_k \tag{4}$$

The specific dissipation rate equation:

$$\frac{\partial}{\partial t}(\rho \omega) + \frac{\partial}{\partial x_i}(\rho \omega u_i) = \frac{\partial}{\partial x_i}\left(\Gamma_\omega \frac{\partial \omega}{\partial x_i}\right) + G_\omega - Y_\omega + D_\omega \tag{5}$$

where the symbols in each formula were denoted in literature [61].

2.2.2. Boundary conditions

The oscillatory flow in the heating tube of a Stirling engine exhibits

two directions during the flow cycle. The flow direction of the working medium reverses at every 180° phase angle. Fig. 2 illustrates that during the entry stage (θ = 0°–180°), the working medium flows from the regenerator outlet to the expansion chamber inlet. In the return stage (θ = 180°–360°), it flows from the expansion chamber outlet to the regenerator inlet. In the numerical simulation, three boundary conditions were defined for the heating tube: cold-end boundary conditions linked to the regenerator end, hot-end boundary conditions linked to the expansion chamber, and wall boundary conditions. The cold-end boundary conditions were specified as a dynamic velocity inlet, as expressed in Eq. (6). The inlet temperature of the working medium in the entry stage was set to 575 K. The hot-end boundary conditions were set at the dynamic pressure outlet, as expressed in Eq. (7), with the inlet temperature of the working medium in the return stage set at 920 K. The temperature of the wall surface was maintained at a constant value of 1000 K. The numerical values of operating parameters in Eqs. (6) and (7) correspond to the Reynolds numbers.

Boundary conditions for the cold end:

$$u = u_{\mathrm{m,max}}\sin(\omega t) \tag{6}$$

Boundary conditions for the hot end:

$$P = P_0 - P_1\cos(\omega t) \tag{7}$$

2.2.3. Parameter definitions

The Reynolds number (Re) for the oscillatory flow included the maximum Re ($\mathrm{Re_{max}}$) and the dynamic Re ($\mathrm{Re_\omega}$) [62]. The former resembles the Reynolds number adopted in steady-state unidirectional flow, whereas the latter represents the ratio of the viscous dissipation timescale to the cycle time of the oscillatory flow. Here, $\mathrm{Re_{max}}$ and $\mathrm{Re_\omega}$ were defined as follows:

$$\mathrm{Re_{max}} = \frac{\rho u_{m,\max} d}{\mu} \tag{8}$$

$$\mathrm{Re_\omega} = \frac{\rho\omega d^2}{\mu} \tag{9}$$

The heat transfer coefficient h and Nusselt (Nu) number, adopted to characterise the heat transfer performance of the heating tube, are defined as follows:

$$h = \frac{q}{T_\mathrm{w} - T_\mathrm{m}} \tag{10}$$

$$\mathrm{Nu} = \frac{hd}{\lambda} \tag{11}$$

The friction factor of working medium in the heating tube was defined as follows:

$$f = \frac{|\Delta P|}{(L/D)\rho u_\mathrm{m}^2/2} \tag{12}$$

In oscillatory flow, the pressure variation at the cold and hot ends of the heating tube alternates between positive and negative due to the periodic change in the flow direction of the working medium. Therefore, when calculating the friction factor, the absolute value of the pressure difference was utilized to facilitate the description.

If a smooth tube were employed instead of three-pronged slant rods, the heat transfer capacity would increase, but the flow friction would unavoidably rise. A performance evaluation criterion (PEC) was employed to quantitatively assess the benefits and costs of heat transfer enhancement. The calculation formula for PEC is shown in Eq. (13), where Nu and Nu_0 represent the Nu numbers of the smooth and enhanced tubes, respectively, while f and f_0 denote the friction factors of the enhanced and smooth tubes, respectively. As the PEC of the enhanced tube varied at different moments (i.e., different phase angles) compared to that of the smooth tube, the average PEC in a cycle under different phase angles was calculated.

$$\mathrm{PEC} = \frac{\mathrm{Nu}/\mathrm{Nu_0}}{(f/f_0)^{1/3}} \tag{13}$$

2.3. Model validation

A fully hexahedral mesh division of the fluid region in the heating tube was conducted, as illustrated in Fig. 3. Prior to formal calculation, five grid sets (2416548, 3080652, 3531570, 4113618, and 4994010) were employed to simulate the heating tube performance. Fig. 4 demonstrates that with an increase in the grid number from 4113618 to 4994010, the difference in the wall average heat flux of the heating tube in a cycle was only 2.51 %. Hence, a grid system with approximately 4.1 million grids was deemed sufficiently dense. Considering computational resources and simulation accuracy, a grid system of 4.1 million approximately was selected for subsequent calculations.

The working medium of the Stirling engine heater undergoes oscillatory motion, consisting of several cycles. Theoretically, flow changes should be consistent across cycles at corresponding phase angles. However, during numerical simulation, initialization settings may influence results in the initial cycles. Therefore, it is essential to conduct cycle-independence verification to determine the appropriate cycle number. Fig. 5 illustrates that flow and heat transfer variations stabilize in each cycle, except for the initial two cycles. For instance, the average difference in heat absorption of the working gas between the 4th and 5th cycles was only 0.45 %. Considering both computational accuracy and time requirements, subsequent analyses were conducted from the 4th cycle.

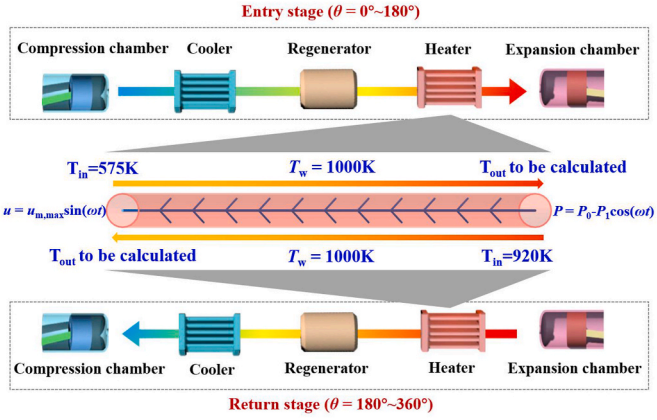

Fig. 2. Schematic diagram of the flow of working medium in the heating tube and the setting of boundary conditions for numerical simulation.

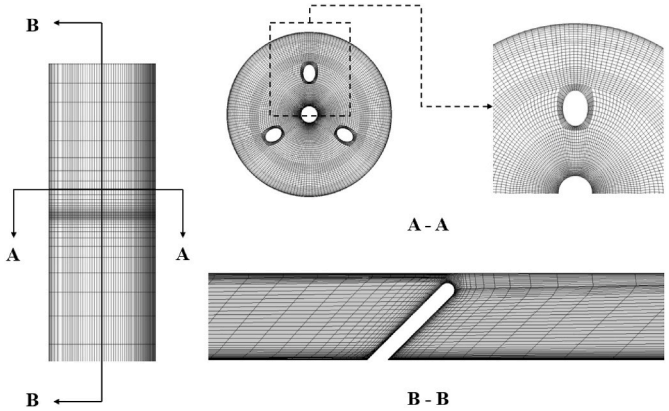

Fig. 3. Schematic diagram of the full hexahedral mesh for the heating tube with three-pronged slant rods.

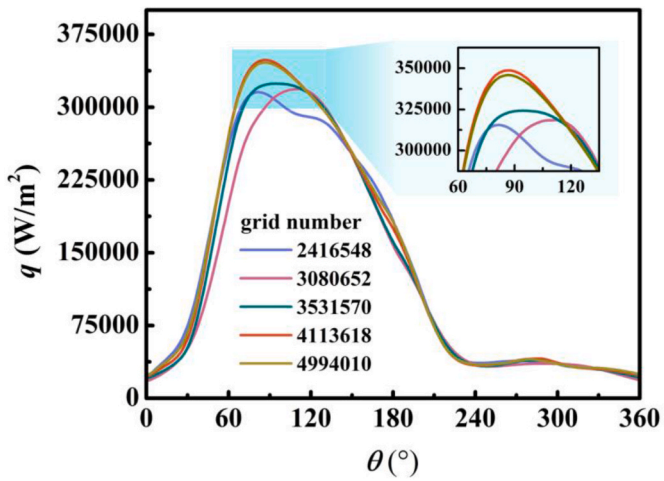

Fig. 4. Mesh independence verification of heating tube.

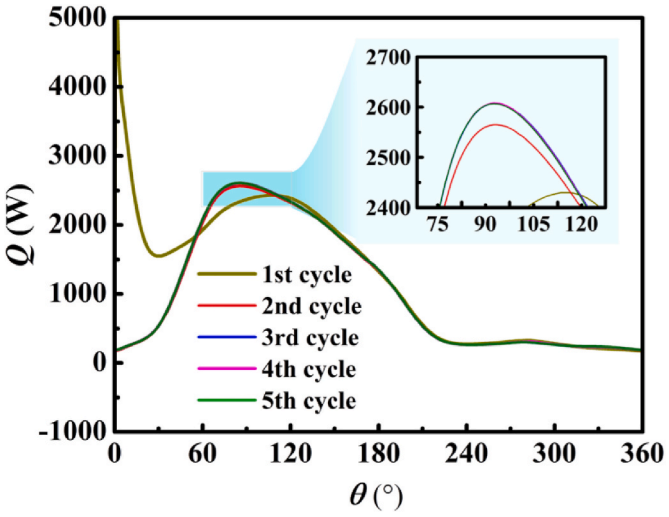

Fig. 5. Cycle independence verification of oscillatory flow for the heating tube.

The simulation results were validated against findings from the literature under identical operating conditions and tube sizes. Fig. 6 illustrates that the simulation results closely align with the experimental and theoretical outcomes reported in the literature [63], affirming the accuracy of the numerical simulation model selected for this study.

3. Results and discussion

3.1. Heat transfer enhancement performance

Fig. 7 illustrates the velocity vector patterns alongside temperature cloud patterns of the fluid in the enhanced tube. The fluid flow direction was altered, and the radial velocity component was induced by the guidance of the slant rods, as depicted by the red arrow in Fig. 7. The velocity vector varied with time (i.e., the phase angle) due to changes in axial pressure gradient and viscous and inertial forces at different moments. At a representative phase angle of 90° for the entry stage, the main flow direction of the working medium aligned with the inclination of the slant rods. From the cross-section at $z = 80$ mm to $z = 150$ mm, the fluid inside the tube was progressively heated by the tube wall, leading to a rise in fluid temperature within the heating tube. During the flow process, the cold fluid in the core region predominantly interacted with the slant rods, as indicated by the white arrows in Fig. 7(a). The tube wall was swept by cold fluid from the core region along with the slant rods, resulting in a reduction in thermal boundary layer thickness and an increase in temperature gradient near the wall. Additionally, due to obstruction by the tube wall, the cold fluid divided into two vortex currents. One vortex current collided with an opposing vortex current generated by the adjacent slant rod. The hot fluid near the wall region was displaced away from the tube wall towards the tube core region, as indicated by the black arrows in Fig. 7(a), thereby facilitating mixing of hot and cold fluids.

At a representative phase angle of 270° for the return stage, the primary flow direction of the working medium opposed the inclination of the slant rods. From the cross-section at z = 220 mm to z = 150 mm, the working medium was gradually heated by the tube wall, leading to an incremental rise in fluid temperature. During this stage, the hot fluid in the boundary flow region initially encounters the slant rods. At this juncture, the hot fluid near the wall is propelled towards the core region under the guidance of the slant rods, as depicted by the white arrows in Fig. 7(b). Conversely, the cold fluid in the core region is compressed and directed towards the tube wall, as indicated by the black arrows in Fig. 7 (b). Thus, counter-vortex structures are formed with opposite spin directions during the entry stage. Consequently, enhanced heat transfer occurs between the hot fluid near the wall and the cold fluid in the core region.

After inserting the three-pronged slant rods into the heating tube, three pairs of vortex structures were formed during both the entry and return stages. These vortex structures were uniformly and symmetrically distributed along the slant rods, extending the fluid's movement paths. This enhancement facilitated improved heat and mass transfer between different regions and resulted in a more uniform temperature distribution.

Fig. 8 illustrates the local streamline of the heating tube with the three-pronged slant rods. The radial cross-sectional streamline reveals the generation of three pairs of symmetric vortices. During the entry stage (e.g., $\theta = 90°$ and $\theta = 150°$), the core of the vortex pair was situated near the tube wall. The higher the velocity (u for $\theta = 90° > u$ for $\theta = 150°$), the closer is the vortex core to the wall. In the circumferential direction, the core of the vortex pair was located near the slant rod, with the vortex core closer to the slant rod at higher velocities. During the return stage (e.g., $\theta = 300°$, $\theta = 330°$), from the radial direction, the core of the vortex pair was located near the central axis of the tube. Here, the higher the velocity (u for $\theta = 300° > u$ for $\theta = 330°$), the closer is the vortex core to the central axis of the tube. In the circumferential direction, the core of the vortex pair was situated farther from the slant rod, near the intermediate line between two adjacent slant rods. Again, at higher velocities, the vortex core approached the intermediate line.

The local axial streamline depicted in Fig. 8 reveals that the incoming working medium experiences disruption caused by the slant rod obstruction. A spiral streamline forms near the slant rod, with its intensity varying based on the velocity of the working medium. Higher velocities (e.g., u for $\theta = 90°$ and u for $\theta = 300°$) result in a less pronounced spiral pattern. As the working medium flows through the slant rod, the spiral streamline gradually reverts to a flat state. Conversely, lower velocities (e.g., u for $\theta = 150°$ and u for $\theta = 330°$) lead to a more pronounced spiral pattern, indicating significant disturbance across a larger region of the working medium post-slant rod traversal. Additionally, small vortices may emerge near the sidewall, as observed at a phase angle of 150°.

Fig. 9 illustrates the temperature cloud patterns of the fluid in the heating tube at the axial cross-section. As shown, the temperature distribution was affected by the inlet fluid temperature. During the entry stage, where the working medium flows from the regenerator end to the expansion chamber end, the inlet temperature was set to 575 K. Conversely, during the return stage, where the working medium flows from the expansion chamber end to the regenerator end, the inlet temperature was set at 920 K. Consequently, the heating-tube temperature during the entry stage was lower than that during the return stage. The inlet velocity of working medium also affected the temperature

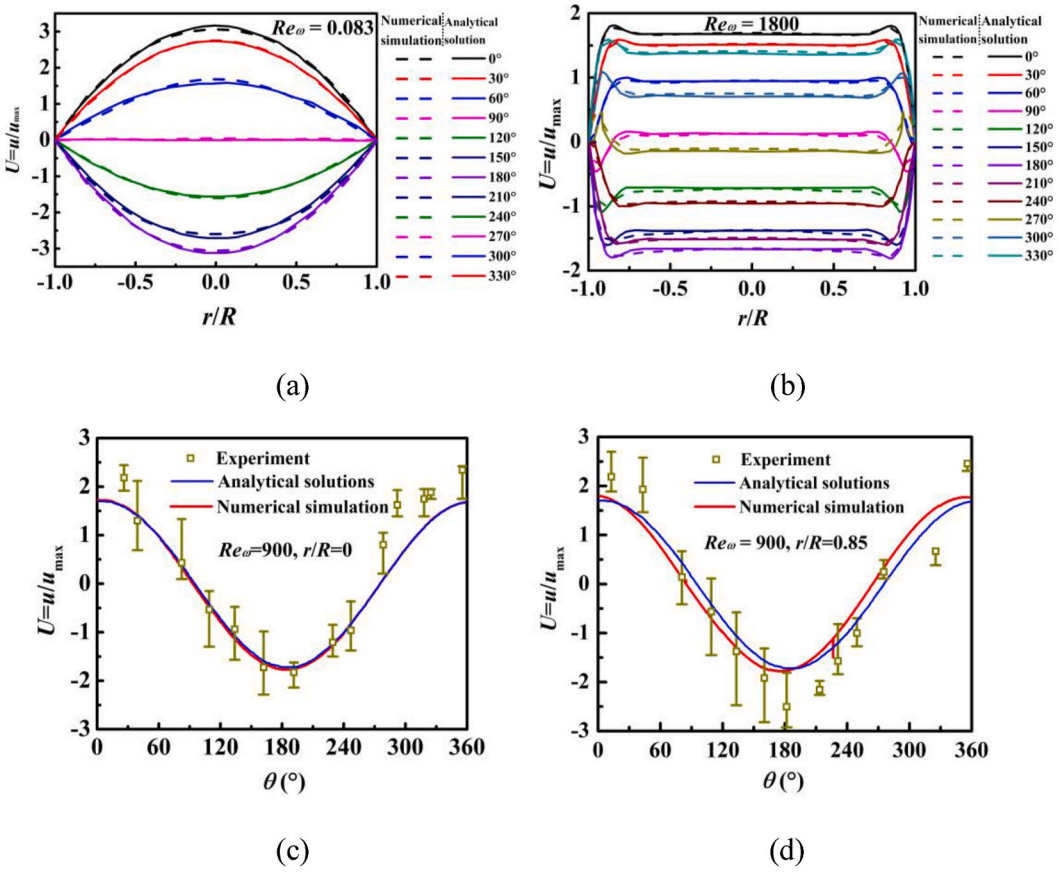

Fig. 6. Comparisons between the numerical simulation results for this study and the experiment results and analytical solutions in literatures [63] (using a smooth tube as the object): (a) The dimensionless velocity change with radial position for $Re_\omega = 0.083$; (b) The dimensionless velocity change with radial position for $Re_\omega = 1800$; (c) The dimensionless velocity change with phase angle for $Re_\omega = 900$, $r/R = 0$; (d) The dimensionless velocity change with phase angle for $Re_\omega = 900$, $r/R = 0.85$.

distribution. A higher inlet velocity amplified the influence of the inlet temperature on the overall temperature distribution in the heating tube, albeit with a time lag (i.e., phase angle lag). For the smooth tube, the isotherms under most phase angles exhibited a parabolic-like pattern, with lower temperatures at the tube axis center and higher temperatures near the tube wall. However, a distinct trend was observed at certain phase angles, such as 30°, where the flow directions of the new incoming fluid in this cycle were opposite to those of the stagnant fluid in the previous cycle, resulting in the collision of two fluid streams.

Fig. 9 (a) and Fig. 9 (b) illustrate that the isotherms were changed by the insertion of the slant rods, disrupting the original parabolic-like isotherm. The temperature distribution discrepancy was noticeable on both the far slant rod side (right side of the tube center axis) and the near slant rod side (left side of the tube center axis). In the far slant-rod area, the temperature distribution resembled that of the smooth tube, albeit with a more uniform temperature distribution. However, in the vicinity of the slant rod, the temperature distribution was segregated into two zones: on-flow and back-flow. Heat transfer in the on-flow zone outperformed that in the back-flow zone, particularly evident during the entry stage due to the larger temperature variation between the tube wall and inlet working medium (425 K), compared to the return stage (80 K). Furthermore, the influence of the three-pronged slant rods on temperature distribution in the heating tube became more pronounced with increasing working-medium velocity for the same process. Comparing Fig. 9 (a) and (b) across all phase angles, it is evident that the heat transfer performance of the tube with the three-pronged slant rods surpassed that of the smooth tube throughout a complete cycle.

Fig. 10 illustrates the *Nu* number of the heating tube over one cycle at various Reynolds numbers. In Fig. 10 (a), the transient *Nu* number for the same type of heating tube exhibits a consistent trend across different Reynolds numbers. Specifically, the transient *Nu* number during the entry stage generally surpasses that during the return stage. For the smooth tube, the transient *Nu* number rises with increasing working-medium velocity, with a phase-angle lag of approximately 15°–30°. However, the enhanced tube presents a more intricate transient *Nu* number curve due to the axial distribution of the three-pronged slanted rods. Both Fig. 10 (a) and Fig. 10 (b) demonstrate that, for both smooth and enhanced tubes, the transient *Nu* number at a specific phase angle and the average *Nu* number over one cycle increase with rising Reynolds numbers. However, for the smooth tube, the amplification of the *Nu* number diminishes with increasing Reynolds numbers. However, for the enhanced tube, the amplification of the *Nu* number tends to be more prominent at low Reynolds numbers and remains relatively constant at higher Reynolds numbers. Moreover, both the transient *Nu* number at any phase angle and the average *Nu* number over one cycle increase after the insertion of the slant rods across different Reynolds numbers, underscoring the effectiveness of the three-pronged slant rods in enhancing heat transfer under oscillatory flow conditions.

Fig. 11 illustrates the *Nu* number distribution of the enhanced tube along the circumferential direction. In Fig. 11 (a), during the entry stage, *Nu* numbers in the regions proximal to the slant rod (i.e. $\Phi = 0°$, 120°, 240°, and their vicinity areas) were higher than those in other positions. Between two adjacent slant rods, the maximum *Nu* number was observed at the centreline, gradually decreasing towards both ends. This indicates that *Nu* number initially rises and then declines with increasing Φ. While during the return stage (Fig. 11 (b)), the *Nu* numbers in the region near the slant rods (i.e. $\Phi = 0°$, 120°, 240°, and their vicinity area) were lower than those in other circumferential positions. Between

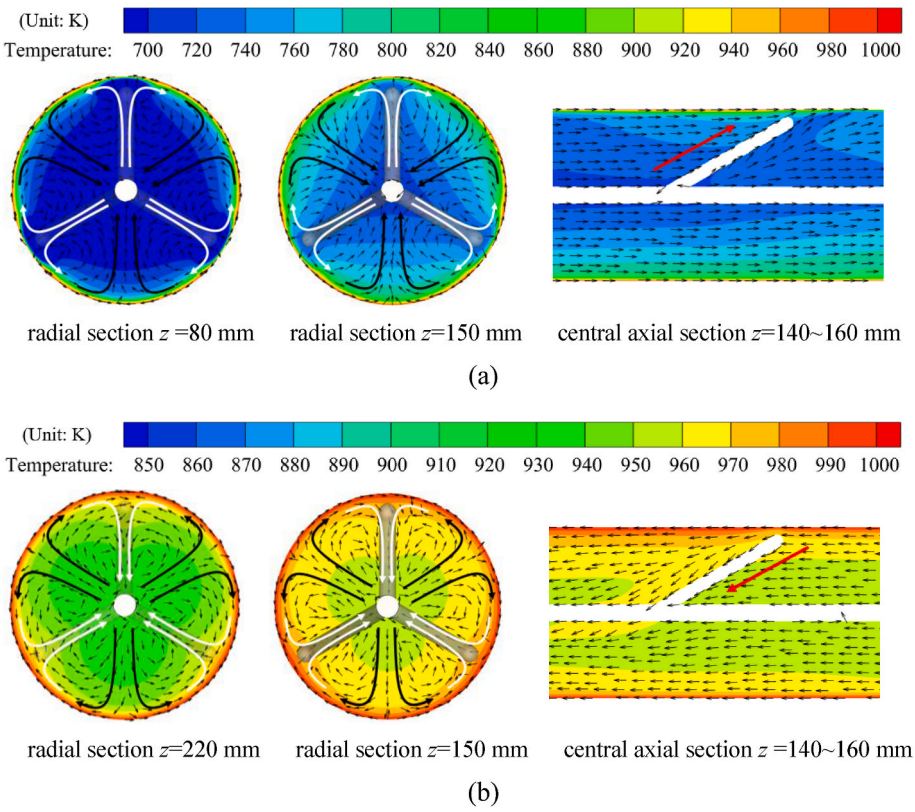

Fig. 7. Velocity vector patterns: (a) entry stage representative phase angle, $\theta = 90°$; (b) return stage representative phase angle, $\theta = 270°$.

two adjacent slant rods, *Nu* number peaked at the centreline and gradually decreased towards the ends, following the same increasing-then-decreasing trend with Φ. This disparity in *Nu* number along the circumferential direction between entry and return stages can be attributed to several factors. During the entry stage, the flow direction aligns with the slant rod inclination, guiding cold fluid from the core region towards the boundary flow area. This reduces the thermal boundary layer near the tube wall, augmenting the temperature gradient and *Nu* number. Conversely, during the return stage, the flow direction opposes the slant rod inclination, directing hot fluid from the boundary area towards the core flow region. This increases the thermal boundary layer near the wall, diminishing the temperature gradient and *Nu* number. The velocity vector patterns (Fig. 7) and streamline diagrams (Fig. 8) corroborate this analysis. Furthermore, for the middle region between two adjacent slant rods, the highest *Nu* number occurs along the central line, both in the entry and return stages. This is attributed to the diverging streams generated by the slant rods, creating a hedging effect in the central line, thereby enhancing heat transfer in the heating tube.

Fig. 12 shows the variation in the *Nu* number along the axial position. The *Nu* number decreases gradually along the flow direction of the working medium at different pitch intervals. During the entry stage, shown in Fig. 12 (a), *Nu* number is at its minimum before the head of the three-pronged slant rods and reaches its maximum value at the tail of the rods within one pitch interval. *Nu* number gradually increases from the head to the tail of the slant rods. Subsequently, from the tail of one set of slant rods to the head of the next, *Nu* number decreases, and this decrease magnitude gradually lessened along the working medium flow direction. This is due to the enhancement of mixing of the working medium at different radial locations near the tail of the slant rods, leading to an increase in *Nu* number. However, as the working medium flows through the slanted rods, the disturbance weakens, resulting in a reduction in *Nu* number. In Fig. 12 (b), during the return stage, within a pitch interval, the *Nu* number peaks when the working medium flows from the tail to the head of the slant rods, while it remains relatively low at other locations (i.e., where the working medium does not flow through the slant rods).

By comparing Fig. 12 (a) and Fig. 12 (b), it is evident that the disturbance created by the slant rods for achieving a uniform temperature distribution of the fluid was more significant and persistent when the working medium flow direction aligned with the slant rod inclination. Comparing phase angles at the entry stage (90° vs. 150°) and return stage (270° vs. 330°), it was observed that the *Nu* number generally increased with higher velocities at the same axial position. However, a contrasting phenomenon was observed in a small area before the head of the three-pronged slanted rod during the entry stage.

Fig. 13 illustrates the transient friction factors for both smooth and enhanced tubes across different phase angles. After inserting the slant rods, the friction factors generally increased compared to smooth tubes throughout most phase angles in a cycle, except during flow direction reversals (approximately at 0° and 180°). This increase resulted from the slant rods obstructing fluid flow and prolonging the working medium's flow path, consequently increasing energy loss per unit length when the working medium flows through the same tube length. During flow reversals, both smooth and enhanced tubes exhibited high friction factors, with friction factors of the smooth tube surpassing those of the enhanced tube. However, this discrepancy did not result from the insertion of the slant rods but rather the lower fluid velocities around this moment. Moreover, the fluid velocity in the smooth tube was lower due to the absence of radial perturbation, resulting in a disproportionately large calculated friction factor (refer to Eq. (12)). To obtain a more accurate assessment of the friction factor cost for the enhanced tube, artificially inflated values occurring around the moment of flow reversal were omitted during the subsequent calculation process for the cycle averages of the friction factor.

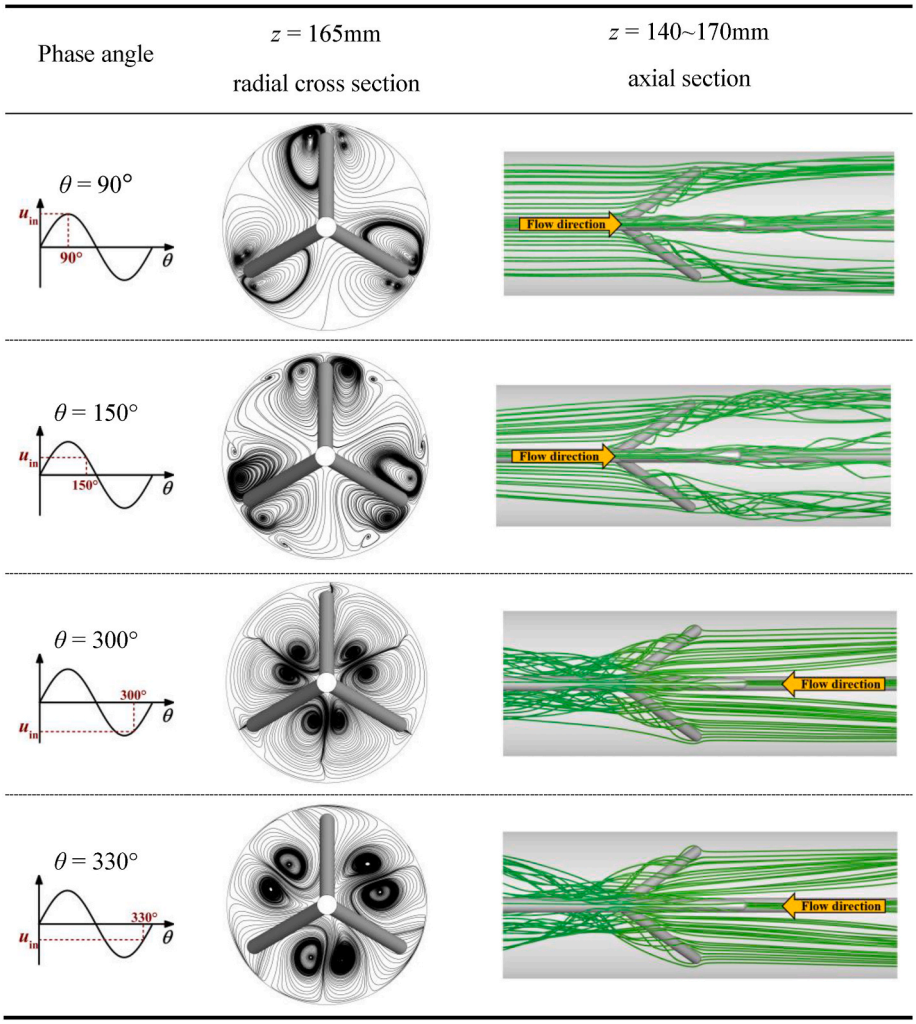

Fig. 8. Local streamline of the fluid in the heating tube with three-pronged slant rods.

3.2. Influence of geometrical parameters of the three-pronged slant rods on heat transfer enhancement performance

3.2.1. Influence of pitch of the three-pronged slant rods

The average outlet temperatures of the smooth tube for the entry and return stages were 865 K and 896 K, respectively. Upon insertion of the three-pronged slant rods, the fluid flow pattern in the heating tube was perturbed, leading to improved heat transfer performance. With specific dimensions (p = 26 mm, l = 3.5 mm, and δ = 30°), the average outlet temperature of the working medium increased to 927 K and 942 K for the entry and return stages, respectively. The number of three-pronged slant rod pairs proved to be a crucial factor affecting heat transfer enhancement, with the pitch size serving as an indicator of the number of such pairs. Fig. 14 depicts the average outlet temperature of the enhanced tube over half a cycle under varying pitches of the three-pronged slant rods. Notably, as the pitch size increased, the average outlet temperatures in both entry and return stages decreased. This trend can be attributed to the reduction in disturbed regions inside the tube with a larger pitch size, thereby limiting the increase in working medium temperature. The outlet temperature serves as a reflection of the heating tube's impact on the energy utilisation of the Stirling engine. A lower outlet temperature during the entry stage suggests a weaker thermal expansion capacity in the expansion chamber, while a lower temperature during the return stage indicates reduced energy recovery in the regenerator for preheating in the subsequent cycle.

Fig. 15 illustrates the temperature cloud patterns of the enhanced tube with varying slant rod pitches. As depicted in Fig. 15 (a), an increase in pitch size led to a reduced probability of disturbance caused by the three-pronged slant rods within the same tube length area, under other certain geometric and operational parameters. Consequently, the mixing of hot fluid near the side-tube wall and cold fluid in the tube core flow area decreased, resulting in a larger tube core area exhibiting a low-temperature state along the axial direction, indicated by the blue coloration. This tendency brought the temperature cloud patterns of the enhanced tube closer to those of the smooth tube. Conversely, for smaller pitches (e.g., p = 26 mm), fluid disturbance increased, causing the high-temperature fluid layer to become thinner, leading to a more uniform temperature distribution inside the heating tube. In this scenario, the heat transfer enhancement capability of the three-pronged slant rods became even more pronounced. Upon comparing Fig. 15(a) and (b), it's evident that the influence mechanism of the pitch of the three-pronged slant rods on heat transfer enhancement during the return stage mirrored that of the entry stage, contingent upon the degree of disturbance at equidistant intervals.

Fig. 16 presents the average *Nu* number, friction factor, and PEC value at a specific height and inclination angle of the three-pronged slant rods. With an increase in pitch, both the average *Nu* number and friction factor exhibited a decreasing trend, while the PEC value initially rose before declining with further increases in pitch. Notably, as the pitch increased from 26 to 42 mm, the *Nu* number experienced a slight reduction, whereas the friction factor exhibited a significant decrease. Consequently, the overall PEC increased from 1.41 to 1.62. Thus, it is

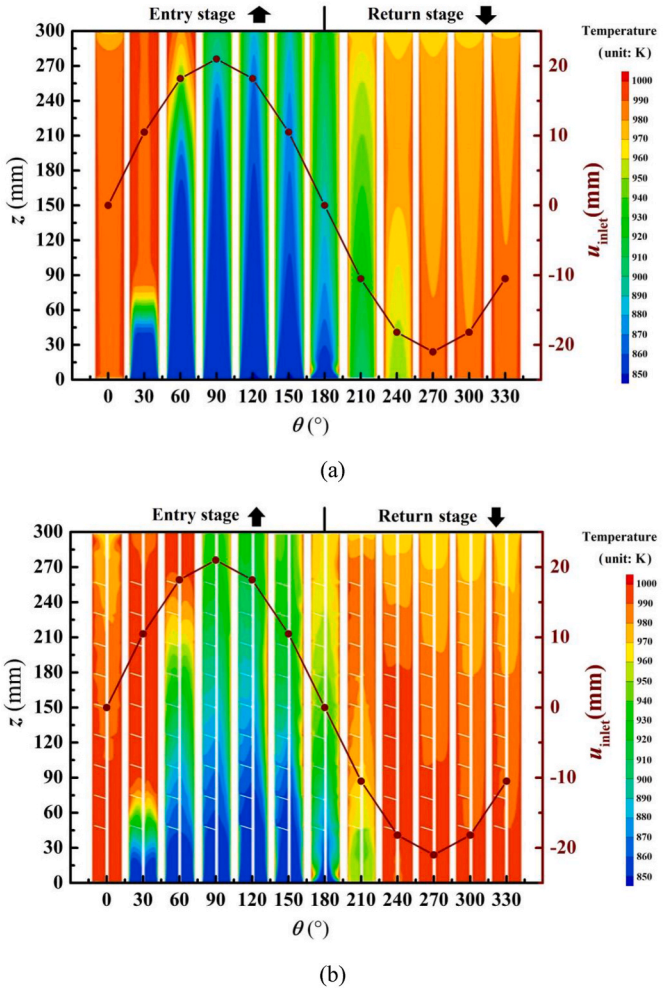

Fig. 9. Temperature contour patterns at the central axial cross section with inlet velocity value of heating tube under different phase angels: (a) smooth tube; (b) tube with three-pronged slant rods.

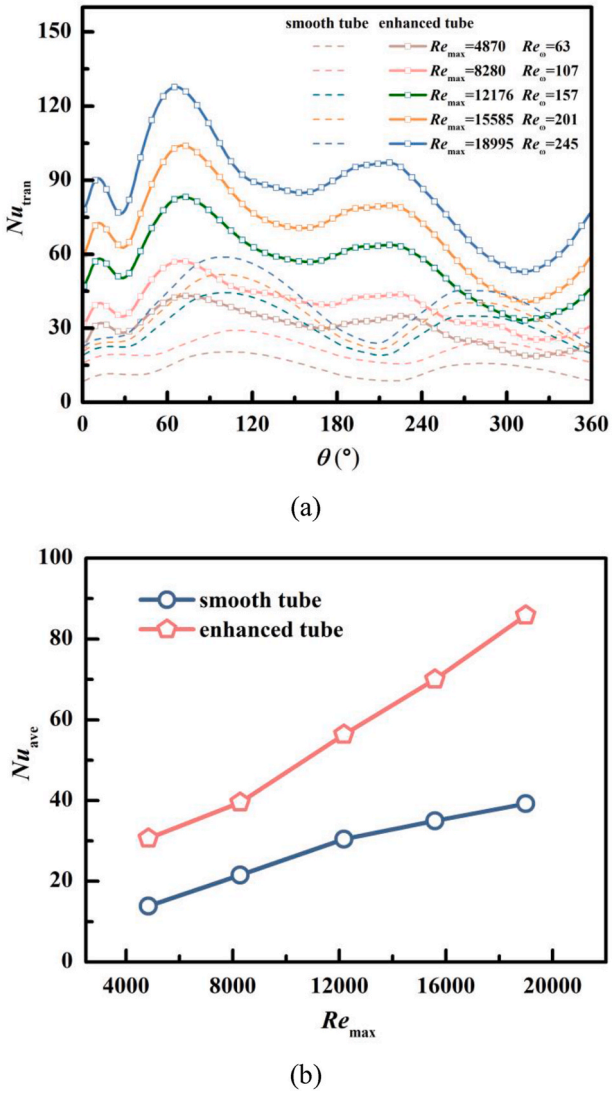

Fig. 10. *Nu* numbers change regular at different Reynolds numbers: (a) the transient *Nu* number; (b) the average *Nu* number.

advisable to opt for a moderate pitch rather than the minimum pitch to achieve the most optimal comprehensive heat transfer enhancement.

3.2.2. *Impact of height of three-pronged slant rods*

Fig. 17 shows the average outlet temperature of the fluid for different three-pronged slant-rod heights in the enhanced tube. At a certain pitch and inclination, the average outlet temperature of the working medium increased with an increase in slant rod height. The increase in the outlet temperature amplitude during the entry stage was greater than that during the return stage. In other words, compared with the working medium flowing into the regenerator, the thermal expansion capacity enhancement of the working medium flowing into the expansion chamber was more significant with an increase in the slant rod height.

Fig. 18 illustrates the temperature-cloud patterns of the enhanced tube at various slant-rod heights. With the three-pronged slant rods, the length increases proportionally with the height at a consistent inclination angle. In Fig. 18(a), during the entry stage, both radial and axial cross-sectional perturbation regions expand as the height increases, which intensifies heat transfer between the cold fluid in the core region and the hot fluid near the tube wall. When the slant rod height is low, the tail of the slant rod is distant from the wall. Consequently, the cold fluid in the core region can only be directed towards the subcore flow region after contacting the slant rod head. This limited interaction diminishes heat exchange with the hot fluid near the sidewall, resulting in notable temperature non-uniformity inside the tube. Fig. 18(b) depicts the return stage, where the elevated slant rod height directs incoming fluid near the wall towards the head from the tail of the slant rods. This facilitates enhanced heat exchange between the hot fluid near the wall and the cold fluid in the core region. However, if the height is too small, the incoming fluid near the wall flows directly around the wall area when passing through the three-pronged slant rods, resulting in a straight flow streamline. Consequently, this limits sufficient heat exchange with the cold fluid in the core region. By considering both Fig. 18 (a) and (b), it is evident that a more pronounced heat transfer enhancement is achieved across the complete flow cycle with increasing slant rod height.

Fig. 19 depicts the average *Nu* number, friction factor, and PEC values for various slant rod heights. As shown, both the average *Nu* number and friction factor exhibit an increase with the slant rod height. Notably, the rate of increase in the *Nu* number is more gradual around smaller (approximately 2.5 mm) and larger (around 3.5 mm) slant rod heights, while it accelerates within the height range of 2.8 mm–3.2 mm. Additionally, as the slant rod height rises, both the friction factor and its rate of increase become more pronounced, particularly nearing a height of 3.5 mm. Regarding the average PEC of the enhanced tube, it initially rises and then declines with increasing slant rod height. Once the height exceeds 3.0 mm, the heat transfer enhancement gain diminishes compared to the friction factor cost induced by the increased slant rod

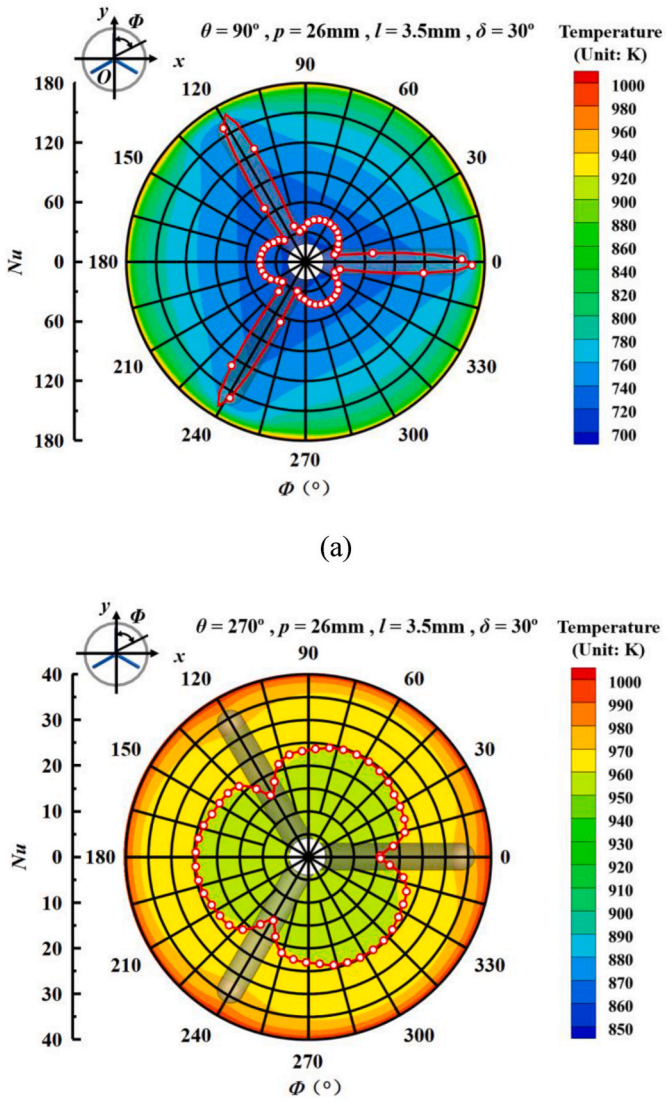

Fig. 11. *Nu* numbers change regular along the circumference at $z = 135$ mm: (a) entry stage representative phase angle, $\theta = 90°$; (b) return stage representative phase angle, $\theta = 270°$.

height.

3.2.3. *Influence of the inclination angle of the three-pronged slant rods*

Fig. 20 illustrates the average outlet temperature of the working medium in a half cycle under various three-pronged slant rod inclination angles. For inclination angles less than 90°, the working medium flows in the same direction as the three-pronged slant rods during the entry stage and in the opposite direction during the return stage, constituting the three-pronged slant-rod forward arrangement. Conversely, when the inclination angle surpasses 90°, the flow streamlines of the working medium oppose those of the slant rods during the entry stage, while aligning with them during the return stage, termed the three-pronged slant-rod backward arrangement.

As depicted in Fig. 20, when the three-pronged slant rods were arranged in a forward configuration, the average outlet temperature of the working medium gradually decreased with an increase in the slant rod inclination angle under a certain pitch and height. Conversely, when the three-pronged slant rods were arranged backward, the average outlet temperature of the working medium gradually increased with an

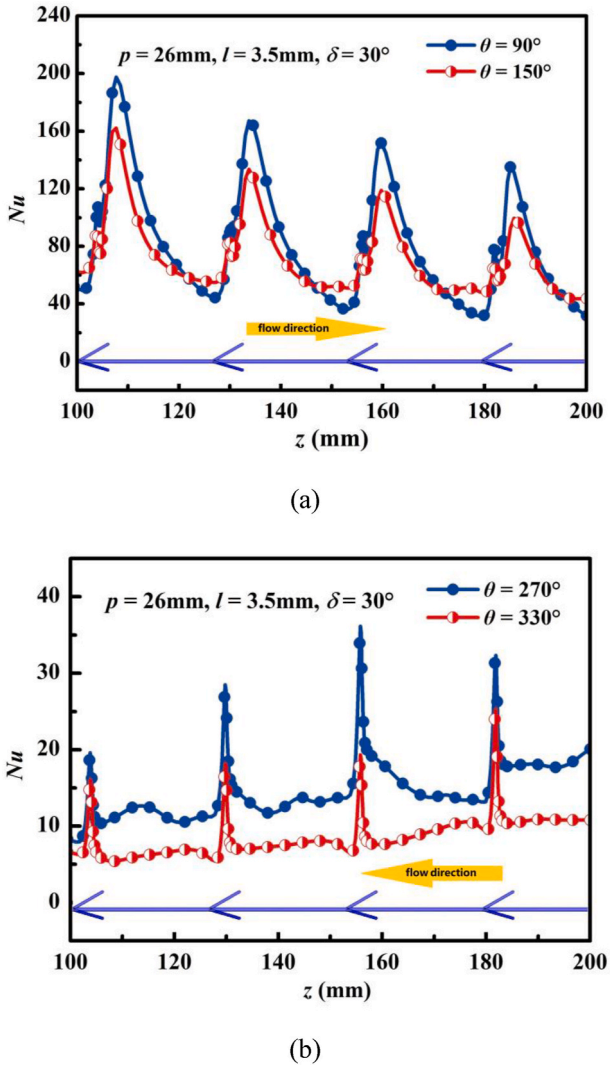

Fig. 12. *Nu* numbers change regular along the axis: (a) entry stage representative phase angle, $\theta = 90°$ and $\theta = 150°$; (b) return stage representative phase angle, $\theta = 270°$ and $\theta = 330°$.

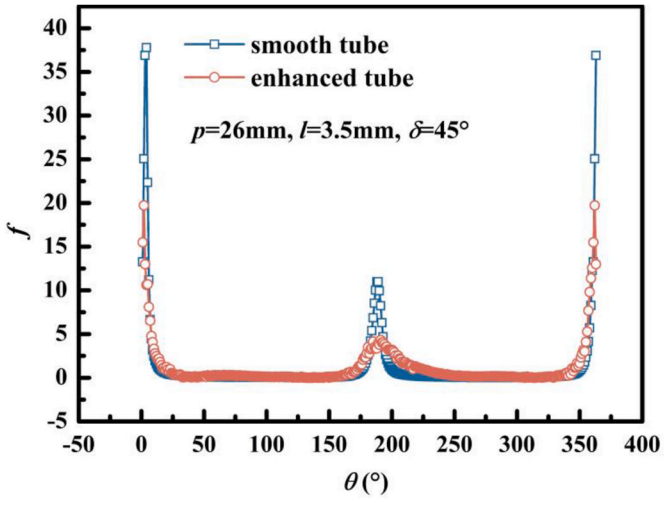

Fig. 13. Friction factors of heating tube change regular with phase angle.

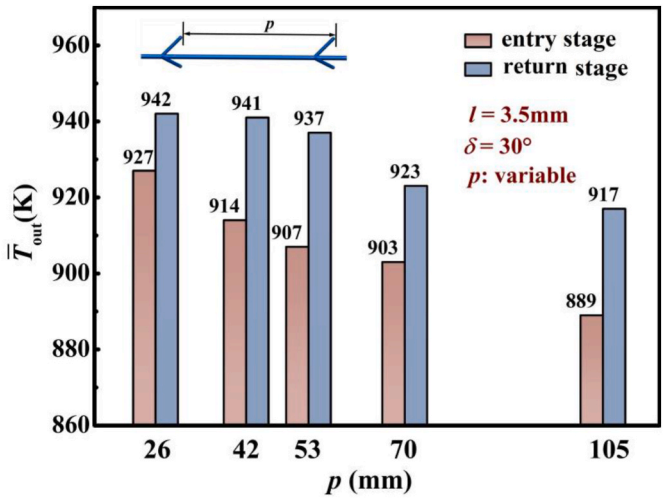

Fig. 14. Average outlet temperature of working gas in half cycle change with the pitch of the three-pronged slant rods.

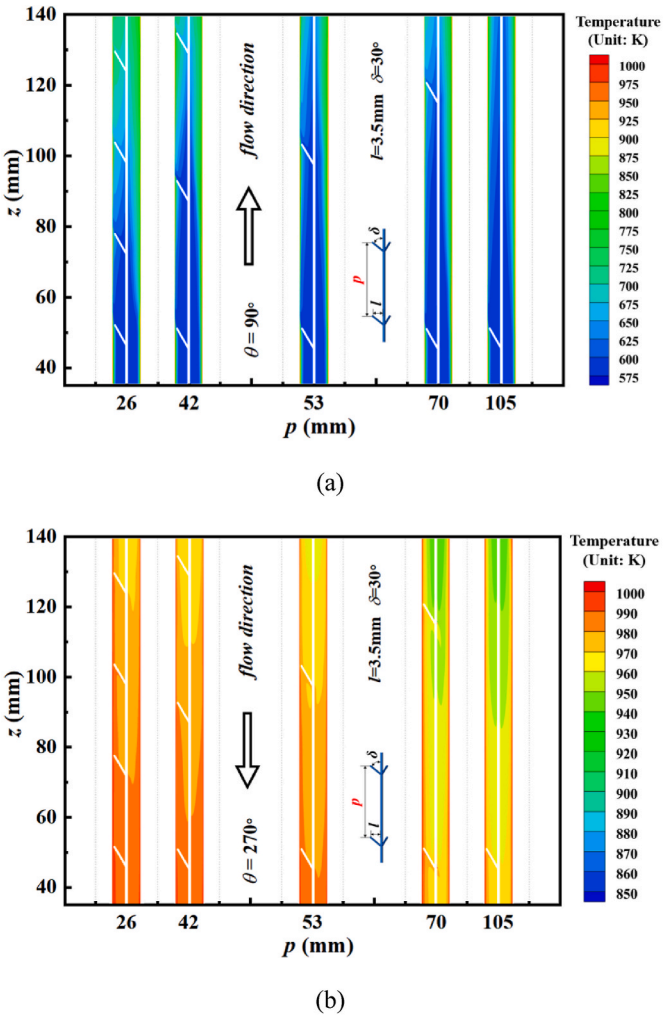

Fig. 15. Temperature cloud patterns at the local axial cross section of enhanced tube under different pitches of three-pronged slant rods: (a) entry stage representative phase angle, $\theta = 90°$; (b) return stage representative phase angle, $\theta = 270°$.

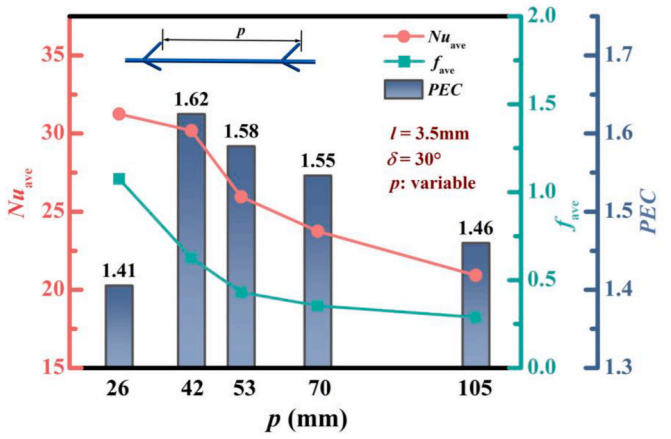

Fig. 16. Average *Nu* number, average friction factor and PEC change with the pitch of the three-pronged slant rods.

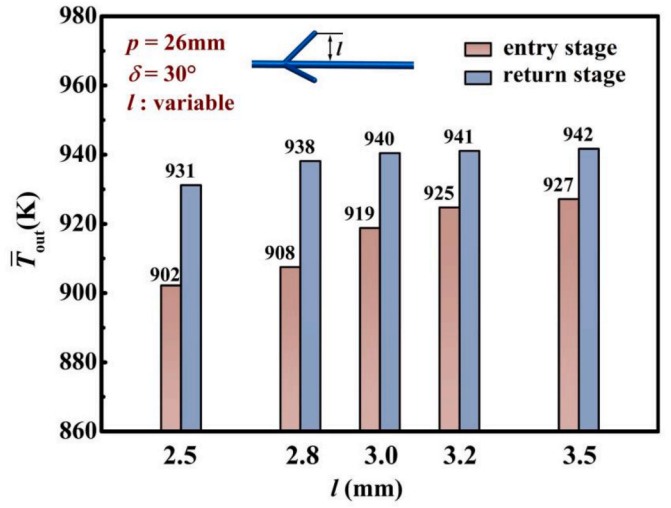

Fig. 17. Average outlet temperature of working medium in half cycle under different three-pronged slant rods heights.

increase in the slant rod inclination angle. Notably, compared to the backward arrangement at corresponding phase angles (e.g., $\delta = 30°$ corresponding to $\delta = 150°$; $\delta = 45°$ corresponding to $\delta = 135°$), the outlet temperature of the working medium was higher when the three-pronged slant rods were arranged in the forward arrangement. For instance, the average outlet temperature of the working medium was 927 K for $\delta = 30°$ and 906 K for $\delta = 150°$. A similar trend was observed during the return stage.

Fig. 21 illustrates the temperature cloud patterns of the enhanced tube in the local central axial cross-section at various inclination angles. As depicted in Fig. 21 (a), when the three-pronged slant rods were arranged in the forward configuration ($\delta < 90°$), the incoming working medium initially contacted the slant rod head. Subsequently, guided by the slant rods, the working medium flowed towards the wall side. With increasing inclination angle, the three-pronged slant rods shortened, thereby reducing the disturbance region in the heating tube. This effect was particularly pronounced at an inclination angle of 90°, where a significant portion of the fluid flowed around the three-pronged slant rods rather than being guided by them. The mixture of hot and cold fluids was constrained by the around flow behaviour, resulting in relatively poor heat transfer performance. Moreover, under a large inclination angle (e.g., $\delta = 90°$), the heat transfer performance near the slant rod side (left side of the central rod) and far slant rod side (right side of

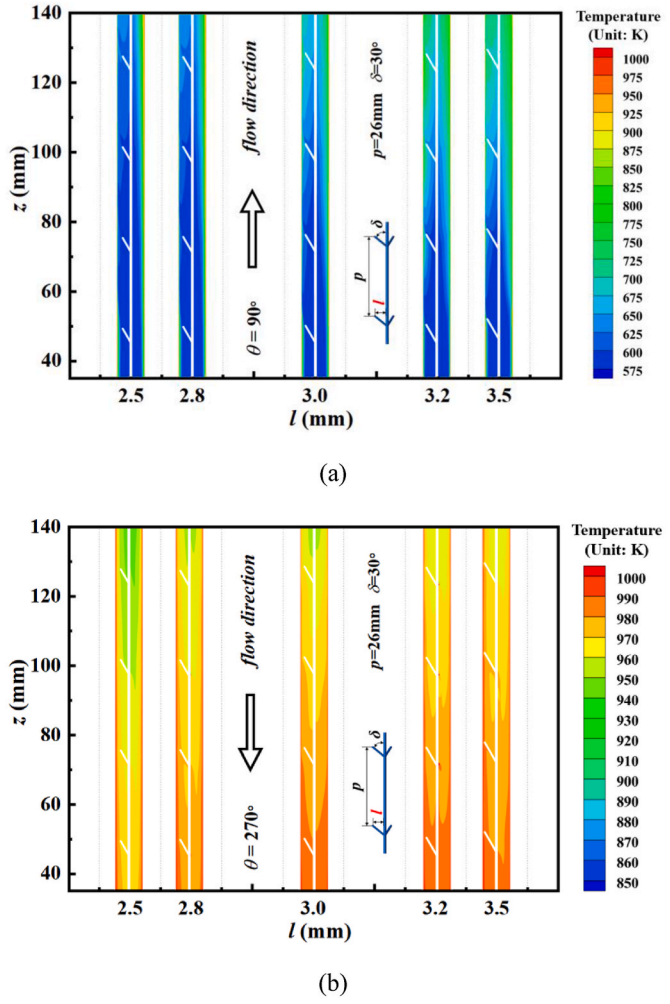

Fig. 18. Temperature cloud patterns of the local axial cross section of the enhanced tube under different heights of the three-pronged slant rods: (a) entry stage representative phase angle, $\theta = 90°$; (b) return stage representative phase angle, $\theta = 270°$.

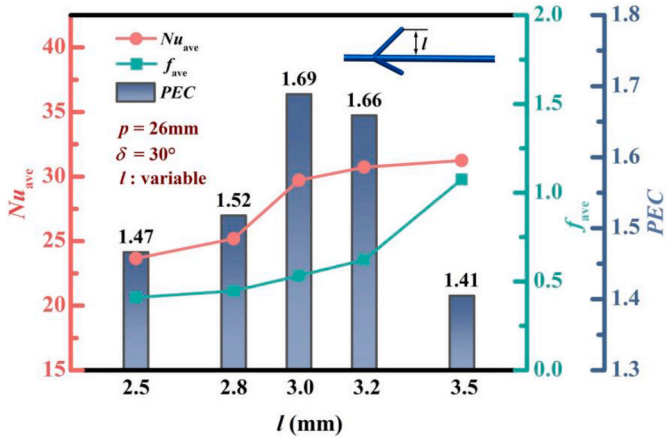

Fig. 19. Average *Nu* number, average friction factor and PEC under different three-pronged slant rods heights.

the central rod) were notably weak. Conversely, in the case of a small inclination angle (e.g., $\delta = 30°$), the superior heat transfer enhancement near the slant rod side also facilitated the heat transfer process on the far slant rod side. This occurred because the working medium in the core

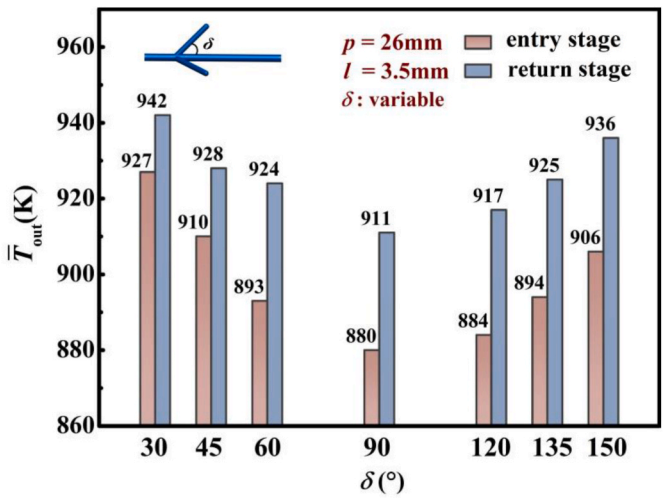

Fig. 20. Average outlet temperature of working gas in half cycle under different three-pronged slant rods inclination angles.

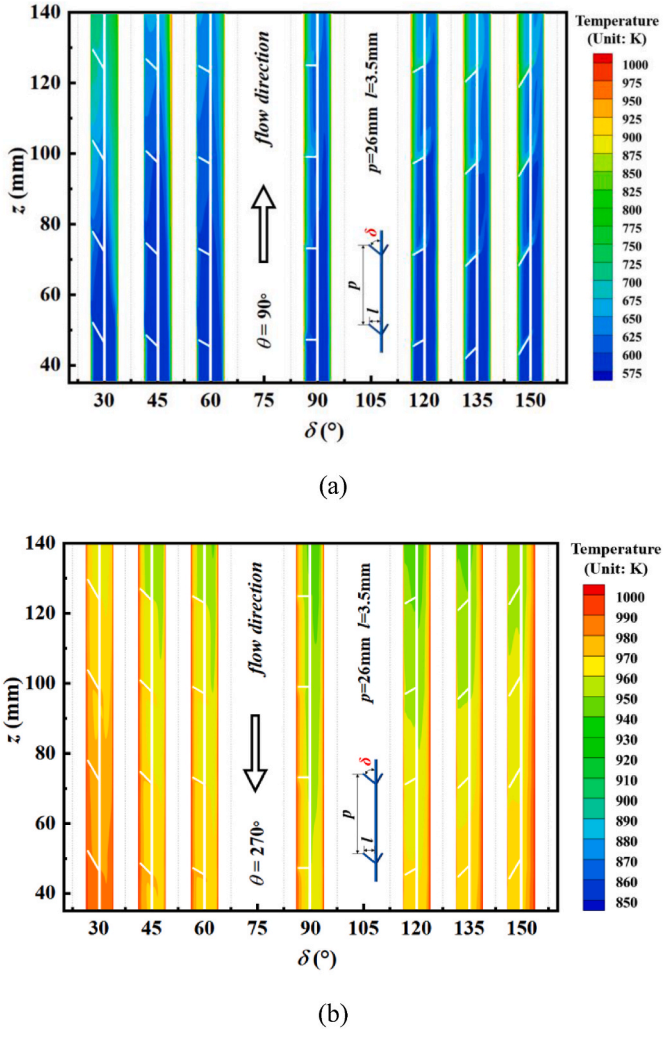

Fig. 21. Temperature cloud patterns of the local axial cross section of the enhanced tube under different inclination angles of the three-pronged slant rods: (a) entry stage representative phase angle, $\theta = 90°$; (b) return stage representative phase angle, $\theta = 270°$.

area was diverted by the slant rods, flowing towards the sidewall area where it was hindered and forced to flow to the two sides. This resulted in the formation of two opposite fluid streams, and the diverging streams with opposite flow directions exhibited hedging behaviour in the centreline of the two slant rods (i.e., the far slant rod side in the figure and the right side of the centre rod). Consequently, energy exchange was promoted (see the radial cross-sectional velocity vectors shown in Fig. 7). Therefore, the heat transfer performance on the far slant rod side was also significant.

When the three-pronged slant rods were arranged in a backward configuration ($\delta > 90°$), heat transfer was enhanced with an increase in the inclination angle of the slant rods, following a mechanism similar to that observed under the forward arrangement. However, better heat transfer was achieved under the forward arrangement compared to the corresponding inclination angles under the backward arrangement (such as $\delta = 30°$ corresponding to $\delta = 150°$). This suggests that the diversion of the slant rods from the head to the tail produced a greater heat transfer enhancement effect than the diversion from the tail to the head.

Fig. 21 (a) and Fig. 21 (b) demonstrate that the impact of the inclination angle of the three-pronged slant rods on heat transfer enhancement during the return stage mirrors that of the entry stage. In vertical and near-vertical configurations, the diversion effect of the slant rods diminishes. Consequently, the working medium flows directly around the slant rods, leading to a reduced heat transfer enhancement performance.

Fig. 22 presents the average *Nu* number, friction factor, and PEC of the enhanced tube across various slant rod inclination angles. When the three-pronged slant rods were positioned in a forward arrangement, the average *Nu* number of the enhanced tube decreased with an increasing inclination angle. Conversely, in a backward arrangement, the average *Nu* number increased with the inclination angle, mirroring the trend observed in the average outlet temperature of the working medium. For the forward arrangement, the average friction factor initially decreased and then increased as the inclination angle increased. This trend was also observed in the backward arrangement. The friction factor was influenced by both the length and obstruction level of the three-pronged slant rods. On one hand, a larger inclination angle resulted in a shorter rod length, reducing the friction factor. On the other hand, a larger inclination angle also increased obstruction, leading to higher radial velocity component and lower axial velocity component, increasing the friction factor. Combined the effects of above two factors, the friction factor exhibited an initial decrease followed by an increase with the increase of the slant rods inclination. Similar to the forward arrangement, the reasons for friction factor changes in the backward arrangement were analogous. Consequently, the PEC values initially increased and then decreased with increasing slant rod inclination angles for both arrangements. The highest PEC value (1.81) was achieved with a pitch of 26 mm, height of 3.5 mm, and inclination angle of 45°.

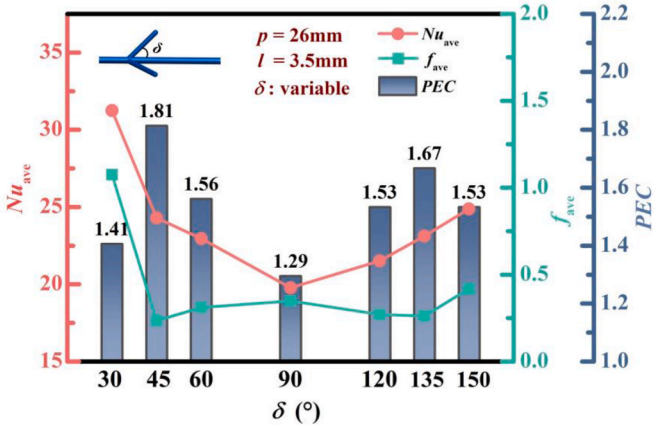

Fig. 22. Average *Nu* number, average friction factor and PEC change under different three-pronged slant rods inclination angles.

The heat transfer enhancement achieved by inserting slant rods into the heating tube was compared with results reported in the literature. Relative to a smooth surface, the PEC values for enhanced surfaces after inserting triangular, rectangular, and curved fins were reported as 1.05, 1.06, and 1.23, respectively [58]. Additionally, a spirally corrugated tube showed a PEC value of 1.38 compared to a smooth tube [59], while a tube inserted with a spiral spring exhibited a PEC value of 1.22 [60]. Furthermore, the PEC of a heat exchanger with porous media reached 1.9, significantly enhancing heater heat transfer performance. However, the widespread application of porous media might be limited due to its tendency to substantially increase flow friction factors. Overall, the insertion of three-pronged slant rods demonstrated superior heat transfer enhancement in the heating tube under oscillatory flow conditions.

4. Conclusions

The heat-transfer enhancement of the heating tube was achieved by inserting three-pronged slant rods. The main conclusions are as follows.

(1) Within the enhanced tube, the insertion of three-pronged slant rods led to the formation of 3 pairs of longitudinal vortex structures. These vortex structures exhibited opposite rotations during the entry and return stages, moving systematically in both circumferential and radial directions at various phase angles. This extended the flow path of the working medium, thereby enhancing heat transfer between the cold fluid in the core region and the hot fluid around the wall-side region.

(2) Following the insertion of the slant rods, there was a noticeable increase in the Nusselt number of the heating tube, which correlated with the Reynolds number. Within the Reynolds number range of 4840~18995 the cycle-averaged Nusselt numbers for the smooth and enhanced tubes ranged from 13.87 to 39.24 and from 30.6 to 85.83, respectively. In the radial section of the enhanced tube, the maximum Nusselt numbers were observed near the slant rods and at the centerline area of two adjacent slant rods during the entry and return stage, respectively. In the axial section, the maximum Nusselt numbers occurred after the working medium flowing over the slant rods during the entry stage and flowing through the slant rods during the return stage. The transient friction factor increased upon insertion of the slant rods into the heating tube, except the reverse moment of working medium flow direction.

(3) The average outlet temperature, average Nusselt number and friction factor all demonstrated an increase with decreasing pitch and increasing height of the three-pronged slant rods. As for the inclination angle, the closer the slant rods were to the vertical state, the weaker the heat transfer enhancement performance. Moreover, the forward arrangement of slant rods proved more effective in enhancing heat transfer compared to the backward arrangement. The average outlet temperature of working medium in the enhanced tube increased 62 K and 46 K during the entry and return stages respectively, in comparison to the smooth tube. The performance evaluation criterion value ranged from 1.29 to 1.81, with the maximum value of 1.81 achieved with a pitch of 26 mm, height of 3.5 mm, and inclination angle of 45°.

CRediT authorship contribution statement

Feng Xin: Writing – review & editing, Writing – original draft, Methodology, Investigation, Funding acquisition, Conceptualization. **Bin Tang:** Writing – original draft, Validation, Methodology, Investigation, Formal analysis. **Bin Zhao:** Writing – review & editing,

Investigation. **Yanfeng Yang:** Writing – review & editing, Funding acquisition. **Wei Liu:** Writing – review & editing, Supervision, Conceptualization. **Zhichun Liu:** Writing – review & editing, Supervision, Conceptualization.

Declaration of competing interest

The authors declare that they have no known competing financial interests or personal relationships that could have appeared to influence the work reported in this paper.

Data availability

Data will be made available on request.

Acknowledgements

This research was supported by the National Natural Science Foundation of China (52206069, 12304491), the Foundation of State Key Laboratory of Coal Combustion (FSKLCCA2310), the Doctoral Scientific Research Foundation of Changsha University of Science and Technology (000303910) and the Natural Science Foundation of Hunan Province, China (2020JJ5590).

Nomenclature

c_p	specific heat (J kg^{-1} K^{-1})
D	inner diameter of the heating tube (mm)
d_1	diameter of the intermediate connecting rod for the three-pronged slant rods insert (mm)
d_2	diameter of the slant rods for the three-pronged slant rods insert (mm)
f	friction factor
h	heat transfer coefficient (W m^{-1} K^{-1})
k	turbulent kinetic energy (m^2 s^{-2})
L	overall length (mm)
l	the height of three-pronged slant rods (mm)
L_1	the length of the heating tube for the end connecting the regenerator (mm)
L_2	intermediate length of the heating tube(mm)
L_3	the length of the heating tube for the end connecting the expansion chamber (mm)
P	pressure (Pa)
p	the pitch of three-pronged slant rods (mm)
P_0	average pressure in a cycle (Pa)
P_1	amplitude of pressure in a cycle (Pa)
Q	heat absorption (W)
q	heat flux (W/m^2)
R	radius (mm)
r	radial position (mm)
Re_ω	kinetic Reynolds number, similar to the Reynolds number in steady flow
Re_{max}	maximum Reynolds number, dimensionless frequency
t	time (s)
T	temperature (K)
U	dimensionless velocity
u	velocity (m s^{-1})
$u_{m,max}$	amplitude of bulk mean velocity (m s^{-1})
z	axial position (mm)

Greek symbols

β	the angle between the two slant rods in the circumference direction (°)
δ	the inclination of three-pronged slant rods (°)
Φ	energy dissipation due to viscosity (W m^{-3}) or the circumferential angle from the y-axis (°)
λ	thermal conductivity (W m^{-1} k^{-1})
μ	viscosity (kg m^{-1} s^{-1})
θ	phase angle (°)
ρ	density (kg m^{-3})
ω	specific dissipation rate(s^{-1}) or angular velocity (rad s^{-1})

subscripts

in	inlet
out	outlet
tran	transient
w	wall
ave	average
m	average
max	maximum

References

[1] İncili V, Karaca Dolgun G, Keçebaş A, et al. Energy and exergy analyses of a coal-fired micro-CHP system coupled engine as a domestic solution. Energy 2023;274:127400.
[2] Szczygieł I, Stanek W, Szargut J. Application of the Stirling engine driven with cryogenic exergy of LNG (liquefied natural gas) for the production of electricity. Energy 2016;105:25–31.
[3] Al-Nimr Md, Khashan SA, Al-Oqla H. Novel techniques to enhance the performance of Stirling engines integrated with solar systems. Renew Energ 2023;202:894–906.
[4] Yan J, Peng Y, Liu Y. Optical performance evaluation of a large solar dish/Stirling power generation system under self-weight load based on optical-mechanical integration method. Energy 2023;264:126386.
[5] Yan J, Peng Y, Liu Y. Wind load and load-carrying optical performance of a large solar dish/stirling power system with 17.7 m diameter. Energy 2023;283:129207.
[6] Schneider T, Müller D, Karl J. A review of thermochemical biomass conversion combined with Stirling engines for the small-scale cogeneration of heat and power. Renew Sust Energy Rev 2020;134:110288.
[7] García D, Suárez M-J, Blanco E, et al. Experimental and numerical characterisation of a non-tubular Stirling engine heater for biomass applications. Sustain Times 2022;14(24):16488.
[8] Acampora L, Continillo G, Marra F, et al. Development of an experimental test rig for cogeneration based on a Stirling engine and a biofuel burner. Int J Energ Res 2020;44(15):12559–71.
[9] Zhili T, Dongjiao Z, Yong L, et al. Modelling and control strategy of a distributed small-scale low-temperature geothermal power generation system. IET Renew Power Gen 2022;17(3):539–54.
[10] Dai Z, Wang C, Zhang D, et al. Design and analysis of a free-piston stirling engine for space nuclear power reactor. Nucl Eng Technol 2021;53(2):637–46.
[11] Qi Y, Sun D, Zhang J. Numerical study on a nuclear-powered Stirling system for space power generation. Appl Therm Eng 2023;233:121140.
[12] Colmenar-Santos A, Zarzuelo-Puch G, Borge-Diez D, et al. Thermodynamic and exergoeconomic analysis of energy recovery system of biogas from a wastewater treatment plant and use in a Stirling engine. Renew Energ 2016;88:171–84.
[13] Al-Nimr Md, Khashan S, Al-Oqla H. A novel hybrid pyroelectric-Stirling engine power generation system. Energy 2023;282:128913.
[14] Chen Y, Yu G, Ma Y, et al. A thermally-coupled cascade free-piston Stirling engine-based cogeneration system. Appl Therm Eng 2024;236:121679.
[15] Chen J, Li X, Dai Y, et al. Energetic, economic, and environmental assessment of a Stirling engine based gasification CCHP system. Appl Energy 2021;281:116067.
[16] Chahartaghi M, Sheykhi M. Energy, environmental and economic evaluations of a CCHP system driven by Stirling engine with helium and hydrogen as working gases. Energy 2019;174:1251–66.
[17] Li D, Qin K, Luo K. Underwater striling engine design with modified one-dimensional model. Int J Nav Archit Ocean Eng 2015;7(3):526–39.
[18] De Moura EF, Henriques IB, Ribeiro GB. Thermodynamic-Dynamic coupling of a Stirling engine for space exploration. Therm Sci Eng Prog 2022;32:101320.
[19] Ghanem CR, Gereige EN, Bou Nader WS, et al. Stirling system optimization for series hybrid electric vehicles. Proc I Mech Eng Part D: J Automobile Eng 2021;236(2–3):407–23.
[20] Flannery B, Finckh O, Berresheim H, et al. Hybrid Stirling engine-adsorption chiller for truck auxiliary power unit applications. Int J Refrig 2017;76:356–66.
[21] Laazaar K, Boutammachte N. Development of a new technique of waste heat recovery in cement plants based on Stirling engine technology. Appl Therm Eng 2022;210:118316.
[22] Catapano F, Perozziello C, Vaglieco BM. Heat transfer of a Stirling engine for waste heat recovery application from internal combustion engines. Appl Therm Eng 2021;198:117492.
[23] Babazadeh MA, Babaelahi M, Saadatfar M. Enhancing solar stirling engine performance through the use of innovative heat transfer fin shapes. Int J Therm Sci 2023;190:108290.
[24] Zhu H, Yang X, Tian R, et al. Numerical study on heat transfer of Stirling engine heater tube with rectangular micro-ribs. Numer Heat Tr B-Fund 2020;78(3):141–59.

[25] Najafi G, Hoseini SS, De Goey LPH, et al. Optimization of combustion in micro combined heat and power (mCHP) system with the biomass-Stirling engine using SiO_2 and Al_2O_3 nanofluids. Appl Therm Eng 2020;169:114936.
[26] Ferreira AC, Silva J, Teixeira S, et al. Assessment of the Stirling engine performance comparing two renewable energy sources: solar energy and biomass. Renew Energ 2020;154:581–97.
[27] Karabulut H, Okur M, Halis S, et al. Thermodynamic, dynamic and flow friction analysis of a Stirling engine with Scotch yoke piston driving mechanism. Energy 2019;168:169–81.
[28] Rahmati A, Varedi-Koulaei SM, Ahmadi MH, et al. Dynamic synthesis of the alpha-type stirling engine based on reducing the output velocity fluctuations using Metaheuristic algorithms. Energy 2022;238:121686.
[29] Yildiz C, Bayata F, Mugan A. Multi-objective optimum design of an alpha type Stirling engine using meta-models and co-simulation approach. Energy Convers Manag 2021;232:113878.
[30] Kim D-J, Park Y, Kim TY, et al. Design optimization of tubular heat exchangers for a free-piston Stirling engine based on improved quasi-steady flow thermodynamic model predictions. Energies 2022;15(9):3326.
[31] El-Ehwany AA, Hennes GM, Eid EI, et al. Development of the performance of an alpha-type heat engine by using elbow-bend transposed-fluids heat exchanger as a heater and a cooler. Energy Convers Manag 2011;52(2):1010–9.
[32] Schneider T, Ruf F, Müller D, et al. Performance of a fluidized bed-fired Stirling engine as micro-scale combined heat and power system on wood pellets. Appl Therm Eng 2021;189:116712.
[33] Błasiak P, Pietrowicz S. A numerical study on heat transfer enhancement via mechanical aids. Int J Heat Mass Transf 2019;140:203–15.
[34] Zhang X, Zhang Y. Experimental study on enhanced heat transfer and flow performance of magnetic nanofluids under alternating magnetic field. Int J Therm Sci 2021;164:106897.
[35] Wang R, Chen T, Qi J, et al. Investigation on the heat transfer enhancement by nanofluid under electric field considering electrophoretic and thermophoretic effect. Case Stud Therm Eng 2021;28:101498.
[36] Wang Z, Diao Y, Zhao Y, et al. Experimental and numerical studies of thermal transport in a latent heat storage unit with a plate fin and a flat heat pipe. Energy 2023;275:127464.
[37] Tian X, Jia H, Zhang J, et al. Heat transfer characteristic of particle flow around the out-wall of different geometries. Energy 2023;280:128217.
[38] Li Y, Yu Q, Yu S, et al. Numerical investigation of pulsating flow structures and heat transfer enhancement performance in spherical corrugated helical tube. Appl Therm Eng 2022;213:118647.
[39] Wang Y-B, Huang L-F, Lan N, et al. Heat transfer enhancement by electrohydrodynamics in wavy channels. Appl Therm Eng 2024;236:121556.
[40] Zhang H, Guo W, Guo L, et al. Experimental study of heat transfer performance in a mini-corrugated pipe coupling nanofluids and pulsating wave. Powder Technol 2023;426:118613.
[41] Dizaji HS, Pourhedayat S, Aldawi F, et al. Proposing an innovative and explicit economic criterion for all passive heat transfer enhancement techniques of heat exchangers. Energy 2022;239:122271.
[42] Chandratre VS, Keste AA, Sane NK. Heat transfer enhancement in a heated tube using tri-partition flow splitters. Mater Today Proc 2021;47:5557–63.
[43] Liu P, Kandasamy R, Ho JY, et al. Experimental study on heat transfer enhancement using combined surface roughening and macro-structures in a confined double-nozzle spray cooling system. Appl Therm Eng 2022;202:117850.
[44] Dizjeh SZ, Brinkerhoff J. Numerical investigations of turbulent heat transfer enhancement in circular tubes via modified internal profiles. Int J Thermofluids 2022;16:100237.
[45] Li Z, Lu D, Wang Z, et al. Analysis on flow and heat transfer performance of SCO_2 in airfoil channels with different fin angles of attack. Energy 2023;282:128600.
[46] Yang C, Liu G, Zhang J, et al. Thermohydraulic analysis of hybrid smooth and spirally corrugated tubes. Int J Therm Sci 2020;158:106520.
[47] Farsi M, Khoshvaght-Aliabadi M, Alimoradi A. A parametric study on heat transfer and pressure drop characteristics of circular tube with alternating flattened flow path. Int J Therm Sci 2021;160:106671.
[48] Hu T, Kwan TH, Zhang H, et al. Thermal performance investigation of the newly shaped vacuum tubes of parabolic trough collector system. Energy 2023;278:127802.
[49] Liu L, Sun T, Cao Y, et al. Experimental and numerical investigation on the flow and heat transfer characteristics of the tube with an integrated internal longitudinal fin. Int J Therm Sc 2023;183:107857.
[50] Xu F, Zhang D, Zhang L, et al. Influence of key geometry parameters on heat transfer and flow resistance properties of toothed internal spiral piece cracking furnace tube. Appl Therm Eng 2022;207:118170.
[51] Zheng N, Zhang K, Chen Q, et al. Novel self-join winglet vortex generators for enhanced heat transfer of turbulent airflow in round tubes. Int Commun Heat Mass 2022;130:105806.
[52] Ghasemian M, Sheikholeslami M, Dehghan M. Performance improvement of photovoltaic/thermal systems by using twisted tapes in the coolant tubes with different cross-section patterns. Energy 2023;279:128016.
[53] Ilori OM, Jaworski AJ, Mao X, et al. Effects of edge shapes on thermal-fluid processes in oscillatory flows. Therm Sci Eng Prog 2021;25:101004.
[54] Rogdakis E, Bitsikas P, Dogkas G, et al. Three-dimensional CFD study of a β-type stirling engine. Therm Sci Eng Prog 2019;11:302–16.
[55] Kuosa M, Saari K, Kankkunen A, et al. Oscillating flow in a stirling engine heat exchanger. Appl Therm Eng 2012;45–46:15–23.
[56] Pan C, Zhang T, Wang J, et al. CFD study of heat transfer and pressure drop for oscillating flow in helical rectangular channel heat exchanger. Int J Therm Sci 2018;129:106–14.
[57] Peng H. Characteristic of oscillating flows and effects on heat and mass transfer of key components in Stirling cycles. Zhejiang University; 2018.
[58] Qi ZL, Wang QJ, Zhang XD, et al. Heat exchange performance of Stirling engine heat exchanger. J Eng therm 2014;35(6):1144–7.
[59] Xin F, Liu Z, Zheng N, et al. Numerical study on flow characteristics and heat transfer enhancement of oscillatory flow in a spirally corrugated tube. Int J Heat Mass Transf 2018;127:402–13.
[60] Xin F, Liu Z, Wang S, et al. Study of heat transfer in oscillatory flow for a Stirling engine heating tube inserted with spiral spring. Appl Therm Eng 2018;143:182–92.
[61] Menter FR, Kuntz M, Langtry R. Ten years of industrial experience with the SST turbulence model. Turb Heat Mass Transf 2003;4(1):625–32.
[62] Xiao G, Chen C, Shi B, et al. Experimental study on heat transfer of oscillating flow of a tubular Stirling engine heater. Int J Heat Mass Transf 2014;71:1–7.
[63] Xiao G, Zhou T, Ni M, et al. Study on oscillating flow of moderate kinetic Reynolds numbers using complex velocity model and phase Doppler anemometer. Appl Energy 2014;130:830–7.